Generation of TeV photons by PeV neutrinos in dense astrophysical environments

Jun-Chen Wang,[1,2,*] Hanlin Song,[3,2,†] Hao Li,[4,‡] Jie Zhu,[4,§] and Bo-Qiang Ma[5,2,‖]

[1]*Department of Physics and Jockey Club Institute for Advanced Study, The Hong Kong University of Science and Technology, Hong Kong SAR, China*

[2]*School of Physics, Peking University, Beijing 100871, China*

[3]*Center for Gravitational Wave Experiment, National Microgravity Laboratory, Institute of Mechanics, Chinese Academy of Sciences, Beijing 100190, China*

[4]*Department of Physics, Chongqing University, Chongqing 401331, China*

[5]*School of Physics, Zhengzhou University, Zhengzhou 450001, China*

(Received 18 November 2025; revised 7 July 2026; accepted 20 August 2026; published 10 September 2026)

Recent observations by IceCube and KM3Net of PeV-scale ultra-high-energy (UHE) neutrinos, together with detections of TeV-PeV photons from various sources such as the Crab Nebula, the Galactic Center, and gamma-ray burst by ground-based observatories including Tibet ASγ, MAGIC, Carpet-3, and LHAASO, point to the existence of extreme astrophysical environments capable of accelerating particles to ultra-high energies. These findings motivate investigations of possible connections between UHE neutrinos and photons in such environments. Theoretically, dense regions surrounding compact objects can efficiently produce UHE neutrinos. In this work, we calculate the production of UHE photons from neutrino-nucleon interactions, and note that if these interactions occur in the outer, optically thin regions of dense environments, the resulting photons could potentially be observed. In our model, an incident neutrino scatters off a nucleon, generating secondary partons that hadronize into pions and subsequently decay into UHE photons. We calculate the resulting photon energy spectra and find that for incident (anti)neutrinos with energies above 1 PeV, the probability of producing photons with energies exceeding 1 TeV is greater than 13%. As a concrete application, we show that this mechanism can quantitatively account for the preburst TeV photons observed in GRB 221009A, providing a natural explanation for both their energies and lead times. These findings establish a plausible mechanism linking UHE neutrino events to gamma-ray observations, providing new insights into hadronic processes in extreme astrophysical environments and supporting multimessenger astronomy studies.

DOI: 10.1103/748y-3vyj

I. INTRODUCTION

Ultra-high-energy (UHE) neutrinos and photons serve as critical messengers for probing extreme astrophysical environments that can accelerate particles to energies far beyond terrestrial accelerators. Recent breakthrough detections have expanded our understanding of these cosmic accelerators: the KM3Net Collaboration reported a 220 PeV neutrino, the highest-energy neutrino ever observed [1], following earlier TeV–PeV neutrino measurements by IceCube [2,3]. Parallel advances in gamma-ray astronomy have yielded equally striking results, including a 300 TeV photon from GRB 221009A (Carpet-3) [4], a 1.4 PeV Galactic photon (LHAASO) [5], and TeV–PeV emissions detected by Tibet ASγ [6] and MAGIC [7]. Together, these observations confirm the existence of cosmic accelerators capable of reaching extreme energy scales, yet the underlying particle acceleration and emission mechanisms remain incompletely resolved [8].

In extreme astrophysical settings such as gamma-ray burst (GRB) progenitors [9], flat-spectrum radio quasars [10], and core-collapse supernovae [11–13], UHE particles are generated via distinct processes. UHE neutrinos typically arise from hadronic interactions: accelerated protons or heavy nuclei collide with ambient matter or radiation fields, triggering proton-proton (pp) or proton-photon ($p\gamma$) reactions that produce charged pions. These pions subsequently decay into PeV-scale neutrinos [14]. UHE photons, by contrast, form through both leptonic and hadronic channels: relativistic electrons generate photons via synchrotron radiation or inverse Compton scattering, while hadronic processes (e.g., pp or $p\gamma$ interactions) produce high-energy pions whose decay yields TeV–PeV photons [15,16].

*Contact author: junchenwang@stu.pku.edu.cn
†Contact author: hanlin@stu.pku.edu.cn
‡Contact author: haolee@cqu.edu.cn
§Contact author: jiezhu@cqu.edu.cn
‖Contact author: mabq@pku.edu.cn

 © 2026 American Physical Society

Multimessenger observations of neutrinos and photons offer unparalleled insights into the physical conditions of cosmic accelerators, yet confirmed high-energy multimessenger events remain scarce. Early examples include MeV-scale neutrino detections from SN 1987A [17] and the Sun [18], while more recently, the blazar TXS 0506 + 056 was associated with a 290 TeV IceCube neutrino [19] and enhanced 80–400 GeV gamma-ray emission (MAGIC) [20]. These observations highlight the need to expand beyond traditional particle production frameworks: UHE neutrinos generated in dense regions can traverse to outer, optically thin layers of astrophysical environments, where they interact with nucleons to produce observable UHE photons—addressing the core limitation of photon escape in conventional models.

In this work, we aim to fill these gaps by modeling UHE photon production via neutrino–nucleon scattering in optically thin astrophysical regions. We consider incident (anti)neutrinos with energies spanning 1 TeV to 220 PeV (consistent with recent IceCube and KM3Net observations) and perform a systematic calculation of the resulting photon energy spectra. Our methodology includes three core steps: (i) computing neutrino-parton cross sections for both charged-current and neutral-current processes; (ii) integrating nucleon parton distribution functions (PDFs) and pion fragmentation functions to derive the neutrino-nucleon interaction cross section for π^0 production; and (iii) calculating the decay rate of π^0 (at given energies) into photons to obtain the photon energy probability distribution. Note that in this work we consider only UHE photons originating from π^0 decay, since for other hadrons the branching ratios of decay channels with photons are very small.[1]

In addition to the microscopic calculation, we further apply our results to a concrete astrophysical scenario by modeling the preburst emission of GRB 221009A, thereby connecting the underlying particle-level process to observable signals.

This paper is arranged as follows. In Sec. II, we present the computational methodology in detail, including the calculations of scattering cross sections and decay rates. We present and discuss the energy distribution of UHE photons from neutrino-nucleon interactions in Sec. III, apply the mechanism to the preburst of GRB 221009A in Sec. IV, and summarize our key conclusions in Sec. V.

II. CALCULATION

Recent multimessenger observations, spanning UHE neutrinos and photons, have proliferated, yet a direct causal link between them remains unestablished. Therefore, quantifying the probability that a single UHE (anti)neutrino produces an observable TeV–PeV photon through charged and neutral current scattering on nucleons is essential for assessing astrophysical scenarios where the neutrino and photon generations are connected, or even causal. In this section, we develop the calculation and derive the neutrino-induced photon-production probability, showing that under plausible source conditions this probability can be substantial.

A. Overview

High-energy photon production from (anti)neutrinos of energy E_ν proceeds in two steps: (i) $\nu/\bar{\nu}$ scatter on nucleons ($N = p, n$) producing partons that hadronize into π^0 with momentum p_π; and (ii) the neutral pions decay via $\pi^0 \to \gamma\gamma$ to photons of energy E_γ. The probability for producing a π^0 with momentum p_π is proportional to the neutrino-nucleon cross section,

$$\sigma_{\nu\to\pi^0}(p_\pi, E_\nu) = \frac{1}{2}\sum_{N,i,i'}\int_0^1 \mathrm{d}x \int_0^1 \mathrm{d}z\, f_i^N(x)\hat{\sigma}_{i,i'}(x,z)D_{i'}^{\pi^0}(z), \quad (1)$$

where x is the parton momentum fraction in the nucleon, z the momentum fraction carried by the hadronized π^0, $f_i^N(x)$ the PDF, $D_{i'}^{\pi^0}(z)$ the fragmentation function (FF), and $\hat{\sigma}_{i\to i'}$ the parton-level cross section, which reads

$$\hat{\sigma}_{i,i'} = \frac{1}{2E_\nu 2E_i|v_\nu - v_i|}\int \frac{\mathrm{d}^3p_{i'}}{(2\pi)^3 2E_{i'}}\frac{\mathrm{d}^3p_l}{(2\pi)^3 2E_l} \times |\mathcal{M}_{i,i'}|^2(2\pi)^4\delta^{(4)}(P_\nu + P_i - P_l - P_{i'}). \quad (2)$$

Here p, P, E, and v denote a particle's three-momentum, four-momentum, energy, and velocity, respectively. In Eq. (2), $\mathcal{M}$ is the parton-level scattering amplitude; explicit expressions are given in Sec. II D.

The photons arise from neutral-pion decay, $\pi^0 \to \gamma\gamma$. The conditional probability $P(E_\gamma|p_\pi)$ follows from the decay rate,

$$\Gamma_{\pi^0\to\gamma}(E_\gamma, p_\pi) = \frac{1}{2}\frac{1}{2E_\pi}\int \frac{\mathrm{d}^3p_\gamma}{(2\pi)^3 2E_\gamma}\frac{\mathrm{d}^3p_{\gamma'}}{(2\pi)^3 2E_{\gamma'}} \times |\mathcal{M}_{\pi^0\to\gamma+\gamma}|^2(2\pi)^4\delta^{(4)}(P_\pi - P_\gamma - P_{\gamma'}), \quad (3)$$

where the factor $1/2$ accounts for identical photons.

To obtain the probability that a photon with energy E_γ is produced by the (anti)neutrino with energy E_ν, denoted as $P(E_\gamma|E_\nu)$, we should obtain the probability $P(p_\pi|E_\nu)$, and $P(E_\gamma|p_\pi)$. Then

$$P(E_\gamma|E_\nu) = \int_0^\infty P(E_\gamma|p_\pi)f(p_\pi|E_\nu)\mathrm{d}p_\pi, \quad (4)$$

[1]For instance, the branching ratio of $\pi^\pm \to \ell^\pm\nu\gamma$ is of order $\mathcal{O}(10^{-4})$, much smaller than the branching ratio of $\pi^0 \to \gamma\gamma$ ($\simeq$98.8%) [21].

where $f(p_\pi|E_\nu) \equiv \mathrm{d}P(p_\pi|E_\nu)/\mathrm{d}p_\pi$ is the probability density function. Since $P(p_\pi|E_\nu) \propto \sigma_{\nu\to\pi^0}$ and $P(E_\gamma|p_\pi) \propto \Gamma_{\pi^0\to\gamma}$, the photon-energy density $f(E_\gamma|E_\nu) \equiv \mathrm{d}P(E_\gamma|E_\nu)/\mathrm{d}E_\gamma$ follows as

$$f(E_\gamma|E_\nu) \propto \int_0^\infty \frac{\mathrm{d}\Gamma_{\pi^0\to\gamma}(E_\gamma, p_\pi)}{\mathrm{d}E_\gamma}\frac{\mathrm{d}\sigma_{\nu\to\pi^0}(p_\pi, E_\nu)}{\mathrm{d}p_\pi}\mathrm{d}p_\pi. \quad (5)$$

In next subsections, we will compute $\mathrm{d}\Gamma_{\pi^0\to\gamma}/\mathrm{d}E_\gamma$ and $\mathrm{d}\sigma_{\nu\to\pi^0}/\mathrm{d}p_\pi$, and then $f(E_\gamma|E_\nu)$ can be solved.

B. Pion decay part

In this section, we compute $\mathrm{d}\Gamma_{\pi^0\to\gamma}/\mathrm{d}E_\gamma$ from the reaction $\pi^0 \to \gamma\gamma$ (Fig. 1). The four-momenta are

$$\begin{aligned} P_\pi &= \left(\sqrt{p_\pi^2 + m_\pi^2}, 0, 0, p_\pi\right), \\ P_\gamma &= (E_\gamma, E_\gamma \sin\theta\cos\phi, E_\gamma \sin\theta\sin\phi, E_\gamma\cos\theta), \\ P_{\gamma'} &= (E_{\gamma'}, p_{\gamma',x}, p_{\gamma',y}, p_{\gamma',z}), \end{aligned} \quad (6)$$

where m_π is the neutral pion mass. Based on the energy-momentum conservation $P_\pi = P_\gamma + P_{\gamma'}$, we have

$$(P_\gamma \cdot P_\gamma) = (P_{\gamma'} \cdot P_{\gamma'}) = 0, \qquad (P_\gamma \cdot P_{\gamma'}) = \frac{m_\pi^2}{2}. \quad (7)$$

Additionally, E_γ can be solved as

$$E_\gamma = \frac{m_\pi^2}{2(\sqrt{p_\pi^2 + m_\pi^2} - p_\pi\cos\theta)}. \quad (8)$$

Then, for θ varies in the region $[0, \pi]$, Eq. (8) indicates that E_γ is constrained in the range

$$\frac{\sqrt{p_\pi^2 + m_\pi^2} - p_\pi}{2} \le E_\gamma \le \frac{\sqrt{p_\pi^2 + m_\pi^2} + p_\pi}{2}. \quad (9)$$

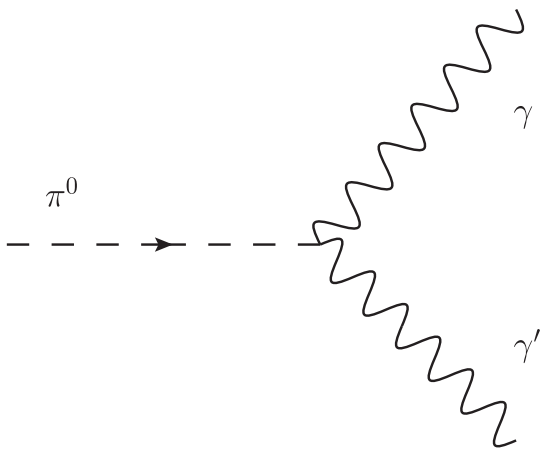

FIG. 1. Feynman diagram for the neutral-pion decay.

After finishing the kinematical analysis, then we focus on the dynamical issue. We solve the amplitude square $|\mathcal{M}_{\pi^0\to\gamma\gamma}|^2$ shown in Eq. (3), which comes from the following effective Lagrangian

$$\mathcal{L} = -\frac{\alpha}{8\pi f_\pi}\epsilon^{\mu\nu\alpha\beta}\pi^0 F_{\mu\nu}F_{\alpha\beta}, \quad (10)$$

where α is fine structure constant, f_π is the pion decay constant, $\epsilon^{\mu\nu\alpha\beta}$ is the Levi-Civita symbol and $F_{\mu\nu} = \partial_\mu A_\nu - \partial_\nu A_\mu$ is the electromagnetic tensor with electromagnetic potential A_μ. Then the amplitude is

$$\mathcal{M}_{\pi^0\to\gamma+\gamma} = i\frac{\alpha}{\pi f_\pi}\epsilon_{\mu\nu\alpha\beta}P_\gamma^\mu \epsilon_k^{*\nu} P_{\gamma'}^\alpha \epsilon_{k'}^{*\beta}, \quad (11)$$

where $\epsilon_k^{*\nu}$ and $\epsilon_{k'}^{*\beta}$ are the photon polarization vectors. Now the amplitude square is solved as

$$|\mathcal{M}_{\pi^0\to\gamma\gamma}|^2 = \frac{\alpha^2 m_\pi^4}{2\pi^2 f_\pi^2}, \quad (12)$$

where the relationship $\sum \epsilon_k^\mu \epsilon_k^{*\nu} = -g^{\mu\nu}$, $\epsilon_{\mu\nu\alpha\beta}\epsilon_{\mu'}{}^{\nu}{}_{\alpha'}{}^{\beta} = 2(g_{\mu\alpha'}g_{\alpha\mu'} - g_{\mu\mu'}g_{\alpha\alpha'})$ has been used.

After deriving the amplitude square Eq. (12), now we can go further to calculate $\mathrm{d}\Gamma_{\pi^0\to\gamma}/\mathrm{d}E_\gamma$. Through Eq. (3), we have

$$\begin{aligned} &\frac{\mathrm{d}\Gamma_{\pi^0\to\gamma}(E_\gamma, p_\pi)}{\mathrm{d}E_\gamma} \\ &= \frac{\alpha^2 m_\pi^4}{64\pi^3 f_\pi^2\sqrt{p_\pi^2 + m_\pi^2}}\int_0^\pi \frac{E_\gamma \sin\theta \mathrm{d}\theta}{\sqrt{E_\gamma^2 + p_\pi^2 - 2p_\pi E_\gamma\cos\theta}} \\ &\quad\times \delta\left(\sqrt{p_\pi^2 + m_\pi^2} - \sqrt{E_\gamma^2 + p_\pi^2 - 2p_\pi E_\gamma\cos\theta} - E_\gamma\right). \end{aligned} \quad (13)$$

For the θ integration in Eq. (13), the kinematics imply that if E_γ lies outside Eq. (9), the equation $\sqrt{p_\pi^2 + m_\pi^2} - \sqrt{E_\gamma^2 + p_\pi^2 - 2p_\pi E_\gamma\cos\theta} - E_\gamma = 0$ has no solution, so $\mathrm{d}\Gamma_{\pi^0\to\gamma}/\mathrm{d}E_\gamma = 0$. If E_γ satisfies Eq. (9), we have

$$\cos\theta = \frac{2E_\gamma\sqrt{p_\pi^2 + m_\pi^2} - m_\pi^2}{2p_\pi E_\gamma}. \quad (14)$$

Then inserting this into Eq. (13), the nonzero $\mathrm{d}\Gamma_{\pi^0\to\gamma}/\mathrm{d}E_\gamma$ is obtained. Finally, the result is

$$\frac{\mathrm{d}\Gamma_{\pi^0\to\gamma}(E_\gamma,p_\pi)}{\mathrm{d}E_\gamma} = \begin{cases} \frac{\alpha^2 m_\pi^4}{64\pi^3 f_\pi^2 p_\pi \sqrt{p_\pi^2+m_\pi^2}}, & \frac{\sqrt{p_\pi^2+m_\pi^2}-p_\pi}{2} \le E_\gamma \le \frac{\sqrt{p_\pi^2+m_\pi^2}+p_\pi}{2}, \\ 0, & \text{otherwise.} \end{cases} \quad (15)$$

With $\mathrm{d}\Gamma_{\pi^0\to\gamma}/\mathrm{d}E_\gamma$ in hand, we next derive $\mathrm{d}\sigma_{\nu\to\pi^0}/\mathrm{d}p_\pi$ in the following subsections.

C. Phase space integration

After obtaining $\mathrm{d}\Gamma_{\pi^0\to\gamma}/\mathrm{d}E_\gamma$, we now turn to $\mathrm{d}\sigma_{\nu\to\pi^0}/\mathrm{d}p_\pi$. Our goal in this section is to solve the phase space integration in Eq. (2). We begin with the kinematics. Here, for convenience we work in the centre-of-mass frame of the (anti)neutrino and nucleon (denoted as the νN-frame in the following). At ultrahigh energies the invariant mass is large, so we neglect the masses of all external particles in the νN-frame. The four-momenta are given as

$$\begin{aligned} &P_\nu = (E_\nu, 0, 0, E_\nu), \qquad P_N = (E_\nu, 0, 0, -E_\nu), \\ &P_i = (xE_\nu, 0, 0, -xE_\nu), \qquad P_l = (E_l, p_{l,x}, p_{l,y}, p_{l,z}), \\ &P_{i'} = \left(\frac{p_\pi}{z}, \frac{p_\pi}{z}\sin\theta\cos\phi, \frac{p_\pi}{z}\sin\theta\sin\phi, \frac{p_\pi}{z}\cos\theta\right), \end{aligned} \quad (16)$$

where the initial parton carries momentum fraction x of the nucleon, and the final-state parton transfers a fraction z to the π^0. From momentum conservation $P_\nu + P_i = P_l + P_{i'}$, we obtain the relations

$$P_\nu \cdot P_i = 2xE_\nu^2, \quad (17)$$

$$P_\nu \cdot P_l = 2xE_\nu^2 - \frac{p_\pi E_\nu}{z}(1-\cos\theta). \quad (18)$$

Additionally, p_π can be solved through the relation $E_l^2 \simeq \sqrt{p_{l,x}^2 + p_{l,y}^2 + p_{l,z}^2}$, with

$$p_\pi = \frac{2xzE_\nu}{(1+x)-(1-x)\cos\theta}. \quad (19)$$

which restricts p_π to the range

$$xzE_\nu \le p_\pi \le zE_\nu. \quad (20)$$

With these kinematics and Eq. (2), we have

$$\frac{\mathrm{d}\hat{\sigma}_{i,i'}(p_\pi,E_\nu)}{\mathrm{d}p_\pi} = \frac{p_\pi}{64\pi x z^2 E_\nu^2}\int_0^\pi \mathrm{d}\theta \sin\theta |\mathcal{M}_{i,i'}|^2 \times \frac{1}{\sqrt{(p_\pi/z)^2 + (1-x)^2E_\nu^2 - 2(1-x)E_\nu(p_\pi/z)\cos\theta}} \times \delta\left((1+x)E_\nu - \frac{p_\pi}{z} - \sqrt{\left(\frac{p_\pi}{z}\right)^2 + (1-x)^2E_\nu^2 - 2(1-x)E_\nu\left(\frac{p_\pi}{z}\right)\cos\theta}\right). \quad (21)$$

As in the decay case, the θ-integration is controlled by kinematics. If p_π lies outside the allowed range (20), the argument of the delta function in Eq. (21) has no solution for $\theta \in [0,\pi]$, giving $\mathrm{d}\hat{\sigma}_{i,i'}/\mathrm{d}p_\pi = 0$. Within the allowed region, $\cos\theta$ is fixed by

$$\cos\theta = \frac{(1+x)p_\pi - 2xzE_\nu}{(1-x)p_\pi}, \quad (22)$$

leading directly to the nonzero result. Now, we obtain the final result of $\mathrm{d}\hat{\sigma}_{i,i'}/\mathrm{d}p_\pi$, which reads

$$\frac{\mathrm{d}\hat{\sigma}_{i,i'}(p_\pi,E_\nu)}{\mathrm{d}p_\pi} = \begin{cases} \frac{|\mathcal{M}_{i,i'}|^2}{64\pi x(1-x)zE_\nu^3}, & xzE_\nu \le p_\pi \le zE_\nu, \\ 0, & \text{otherwise.} \end{cases} \quad (23)$$

With this in hand, we then compute $|\mathcal{M}_{i,i'}|^2$ in Sec. II D to obtain the final $\mathrm{d}\hat{\sigma}_{i,i'}/\mathrm{d}p_\pi$.

D. Electroweak part

In this section we compute the amplitude squares $|\mathcal{M}_{i,i'}|^2$ that enter Eq. (23). (Anti)neutrino-parton scattering proceeds through two types of electroweak interactions: charged-current (CC) processes mediated by W bosons and neutral-current (NC) processes mediated by Z bosons. Representative Feynman diagrams for each class are shown in Fig. 2.

For the CC process in the left panel of Fig. 2, the amplitude square is

$$|\mathcal{M}_{d,u}|^2 = |V_{ud}|^2 \frac{e^4}{\sin^4\theta_w} \times \frac{P_\nu\cdot P_i(m_d^2 - m_e^2 - m_u^2 + 2P_\nu\cdot P_i)}{(m_W^2 - m_e^2 + 2P_\nu\cdot P_l)^2}. \quad (24)$$

Here e is the electric charge, θ_w is the weak mixing angle ($\sin^2\theta_w \simeq 0.23$), and V_{ud} is a CKM matrix element.

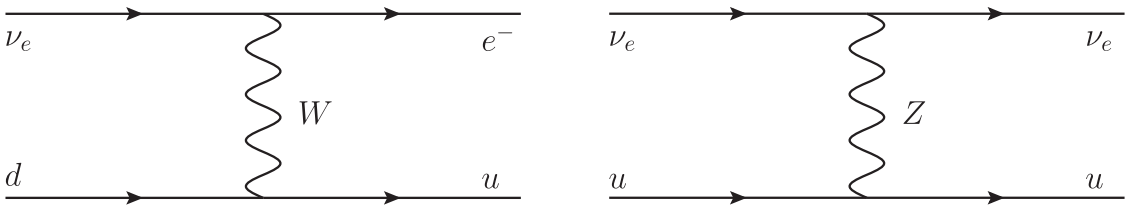

FIG. 2. Representative electroweak diagrams for neutrino-parton scattering: left: charged-current process mediated by a W boson; right: neutral-current process mediated by a Z boson.

For the NC process in the right panel of Fig. 2, we obtain

$$|\mathcal{M}_{u,u}|^2 = \frac{e^4}{\cos^4\theta_w}\frac{1}{18(m_Z^2+2P_\nu\cdot P_l)^2} \times [4P_\nu\cdot P_l(m_u^2(3\csc^2\theta_w-4)-8P_\nu\cdot P_i) + (9\csc^4\theta_w-24\csc^2\theta_w+32)(P_\nu\cdot P_i)^2 + 16(P_\nu\cdot P_l)^2]. \quad (25)$$

Equations (24) and (25) correspond to two representative channels. A complete list of all relevant processes and their amplitude squares is given in the Appendix.

To match the kinematic setup used in Sec. II C, we now evaluate these amplitudes in the νN frame, where particle masses can be neglected. Substituting Eqs. (17), (18), and (22) into the amplitude squares, yields

$$|\mathcal{M}_{d,u}|^2 = \frac{8e^4E_\nu^4|V_{ud}|^2(x-1)^2x^2z^2}{\sin^4\theta_w[4xE_\nu(xzE_\nu-p_\pi)+z(x-1)m_W^2]^2}, \quad (26)$$

$$|\mathcal{M}_{u,u}|^2 = \frac{2e^4x^2E_\nu^2}{9\cos^4\theta_w[4zx^2E_\nu^2-4xE_\nu p_\pi+z(x-1)m_Z^2]^2} \times [16(E_\nu^2z^2(x^2-2x+2)-2zE_\nu p_\pi+p_\pi^2) + 3z^2(x-1)^2E_\nu^2\csc^4\theta_w(8\cos^2\theta_w-5)]. \quad (27)$$

Finally, substituting (26) and (27) into Eq. (23) gives the corresponding contributions to $\mathrm{d}\hat{\sigma}_{i,i'}/\mathrm{d}p_\pi$.

E. PDF and fragmentation function

In this section we briefly summarize the PDFs and FFs that enter the total cross section $\sigma_{\nu\to\pi^0}$ in Eq. (1).

PDFs describe the interior structure of hadrons in deep-inelastic scattering: they give the probability of finding a parton carrying a momentum fraction x of the parent hadron. Because PDFs are nonperturbative, they must be extracted from data rather than computed directly in perturbative QCD. In our calculation, the relevant hadrons are protons and neutrons, and we include the quark flavors u, $\bar{u}$, d, $\bar{d}$, s, and $\bar{s}$. For numerical input we use the PDF sets of Refs. [22,23]; a general review can be found in Ref. [24].

Fragmentation functions describe the hadronization of an energetic parton into final-state hadrons. They encode the probability that a parton produces a hadron carrying a momentum fraction z of the original parton. Like PDFs, FFs are nonperturbative quantities extracted from experiment, with more details discussed in Refs. [25–29]. In this work we adopt the parametrization of Ref. [27], where the FF for producing a π^+ is modeled by

$$D_i^{\pi^+}(z) = \frac{N_i z^{\alpha_i}(1-z)^{\beta_i}[1+\gamma_i(1-z)^{\delta_i}]}{B[2+\alpha_i,\beta_i+1]+\gamma_i B[2+\alpha_i,\beta_i+\delta_i+1]}, \quad (28)$$

with $B[a,b]$ the Euler beta function. The FFs for π^- follow from charge conjugation, e.g., $D_u^{\pi^-}(z)=D_{\bar{u}}^{\pi^+}(z)$, and the neutral-pion FF is obtained through $D_i^{\pi^0}(z)=[D_i^{\pi^+}(z)+D_i^{\pi^-}(z)]/2$.

The fitted parameters for Eq. (28) are listed in Table I. Additional relations used in our calculation include [27]

$$D_{\bar{u}}^{\pi^+}(z)=D_d^{\pi^+}, \qquad D_s^{\pi^+}(z)=D_{\bar{s}}^{\pi^+}(z),$$
$$D_{i+i'}^{\pi^+}(z)=D_i^{\pi^+}(z)+D_{i'}^{\pi^+}(z), \quad (29)$$

which, together with Table I, allow us to obtain all parton FFs needed for π^0 production.

F. Final expression

With all ingredients prepared, the probability density for producing a photon from an incident (anti)neutrino is given by

$$f(E_\gamma^{\mathrm{lab}}|E_\nu^{\mathrm{lab}}) \propto \int_0^\infty \frac{\mathrm{d}\Gamma_{\pi^0\to\gamma}(E_\gamma^{\nu N},p_\pi^{\nu N})}{\mathrm{d}E_\gamma^{\nu N}}\frac{\mathrm{d}\sigma_{\nu\to\pi^0}(p_\pi^{\nu N},E_\nu^{\nu N})}{\mathrm{d}p'_\pi}\mathrm{d}p_\pi^{\nu N}, \quad (30)$$

TABLE I. Fitted parameters $(N_i,\alpha_i,\beta_i,\gamma_i,\delta_i)$ for the fragmentation function in Eq. (28), taken from Ref. [27]. These parameters determine the π^0 FFs follow from charge conjugation, Eq. (29) and $D_i^{\pi^0}(z)=[D_i^{\pi^+}(z)+D_i^{\pi^-}(z)]/2$ as described in the text.

Parton i	N_i	α_i	β_i	γ_i	δ_i
$u+\bar{u}$	0.387	−0.388	0.910	7.15	3.96
$d+\bar{d}$	0.388	−0.388	0.910	7.15	3.96
$\bar{u}=d$	0.105	1.649	3.286	49.95	8.67
$s+\bar{s}$	0.273	1.449	3.286	49.95	8.67

where the ingredients are

$$\frac{d\Gamma_{\pi^0\to\gamma}(E_\gamma,p_\pi)}{dE_\gamma} = \begin{cases} \frac{\alpha^2 m_\pi^4}{64\pi^3 f_\pi^2 p_\pi \sqrt{p_\pi^2+m_\pi^2}}, & \frac{\sqrt{p_\pi^2+m_\pi^2}-p_\pi}{2} \le E_\gamma \le \frac{\sqrt{p_\pi^2+m_\pi^2}+p_\pi}{2}, \\ 0, & \text{otherwise.} \end{cases} \quad (31)$$

$$\frac{d\sigma_{\nu\to\pi^0}(p_\pi,E_\nu)}{dp_\pi} = \frac{1}{2}\sum_{N,i,i'}\int_0^1 dx \int_0^1 dz\, f_i^N(x)\frac{d\hat{\sigma}_{i,i'}(p_\pi,E_\nu,x,z)}{dp_\pi} D_{i'}^{\pi^0}(z), \quad (32)$$

$$\frac{d\hat{\sigma}_{i,i'}(p_\pi,E_\nu,x,z)}{dp_\pi} = \begin{cases} \frac{|\mathcal{M}_{i,i'}|^2}{64\pi x(1-x)zE_\nu^3}, & xzE_\nu \le p_\pi \le zE_\nu, \\ 0, & \text{otherwise.} \end{cases} \quad (33)$$

The required inputs: PDFs $f_i^N(x)$, FFs $D_i^{\pi^0}(z)$, and amplitudes $|\mathcal{M}_{i,i'}|^2$, are provided in Secs. II D, II E, the Appendix, and Refs. [22,23,27].

Note that in Eq. (30) we use superscripts to distinguish quantities in the νN-frame and laboratory frame. Since Eqs. (31)–(33) are constructed in the νN frame, while the observable probability density is defined in the laboratory frame, a Lorentz transformation is required to relate $(E_\nu^{\rm lab}, E_\gamma^{\rm lab})$ to $(E_\nu^{\nu N}, E_\gamma^{\nu N})$.

In the laboratory frame, nucleons are effectively at rest: their thermal energy is $\mathcal{O}(\mathrm{MeV})$ in optically thin astrophysical regions [30], far below the nucleon mass $m_N \simeq 1$ GeV. The relative velocity between the two frames is therefore

$$v = \frac{E_\nu^{\rm lab}}{E_\nu^{\rm lab}+m_N}. \quad (34)$$

Additionally, Refs. [31,32] demonstrate that UHE photons and neutrinos originating from the same source propagate nearly collinearly. Thus both energies transform in the same way,

$$E_{\nu/\gamma}^{\rm lab} \to E_{\nu/\gamma}^{\nu N} = E_{\nu/\gamma}^{\rm lab}\sqrt{\frac{1-v}{1+v}}. \quad (35)$$

To summarize, in this section we have assembled all ingredients needed to compute the conditional probability density $f(E_\gamma^{\rm lab}|E_\nu^{\rm lab})$: the $\pi^0\to\gamma\gamma$ decay rate, the (anti) neutrino induced π^0 production cross section, the underlying electroweak matrix elements, and the nonperturbative PDFs and FFs. Together with the Lorentz transformation between the νN-frame and the laboratory frame, Eqs. (30)–(33) fully determine the photon production probability from an incident (anti)neutrino of energy E_ν. In the next section we evaluate these expressions numerically and explore the resulting E_γ distributions and their phenomenological implications for UHE astrophysics.

III. RESULTS

With the derivations in Sec. II, we can now evaluate the probability distribution for photon production induced by UHE neutrinos and antineutrinos. The results are shown in Fig. 3. The upper (lower) panels correspond to neutrinos (antineutrinos), while the left and right panels display the probability density functions and cumulative distribution functions, respectively. As illustrated in Fig. 3, high-energy (anti)neutrino-nucleon scattering has a sizable probability of producing energetic photons.

Figure 3 exhibits two notable features of the photon distribution:

(i) The probability density is symmetric in $\log E_\gamma$.
(ii) The lower bound on E_γ is nearly independent of the incident (anti)neutrino energy E_ν.

We now explain these features analytically. For clarity, we use superscripts to distinguish quantities defined in different frames.

To explain the symmetry of the photon probability density function, we focus on Eqs. (30)–(33). These show that the dependence of $f(E_\gamma^{\rm lab}|E_\nu^{\rm lab})$ on $E_\gamma^{\rm lab}$ (or equivalently on $E_\gamma^{\nu N}$) arises solely through the kinematic constraint $(\sqrt{(p_\pi^{\nu N})^2+m_\pi^2}-p_\pi^{\nu N})/2 \le E_\gamma^{\nu N} \le (\sqrt{(p_\pi^{\nu N})^2+m_\pi^2}+p_\pi^{\nu N})/2$. In other words, $E_\gamma^{\nu N}$ only alters the integration domain in Eq. (30), but not the integrand. This constraint implies that the integral in Eq. (30) has a lower limit $p_{\rm low}^{\nu N}$, which depends on $E_\gamma^{\nu N}$ and is given by,

$$p_{\rm low}^{\nu N} = \frac{|m_\pi^2 - 4(E_\gamma^{\nu N})^2|}{4E_\gamma^{\nu N}}. \quad (36)$$

Crucially, both $E_\gamma^{\nu N}$ and $m_\pi^2/(4E_\gamma^{\nu N})$ lead to the same $p_{\rm low}^{\nu N}$. Therefore, the integrand and integration region in Eq. (30) are identical for these two energies. Giving

$$f(E_\gamma^{\nu N}|E_\nu^{\nu N}) = f\left(\frac{m_\pi^2}{4E_\gamma^{\nu N}}\middle| E_\nu^{\nu N}\right), \quad (37)$$

where the two quantities satisfy $\log E_\gamma^{\nu N} + \log(m_\pi^2/4E_\gamma^{\nu N}) = 2\log(m_\pi/2)$, proving that f is symmetric in $\log E_\gamma^{\nu N}$ around $m_\pi/2$.

In the laboratory frame, the Lorentz transformation in Eqs. (34) and (35) shifts the symmetry axis to

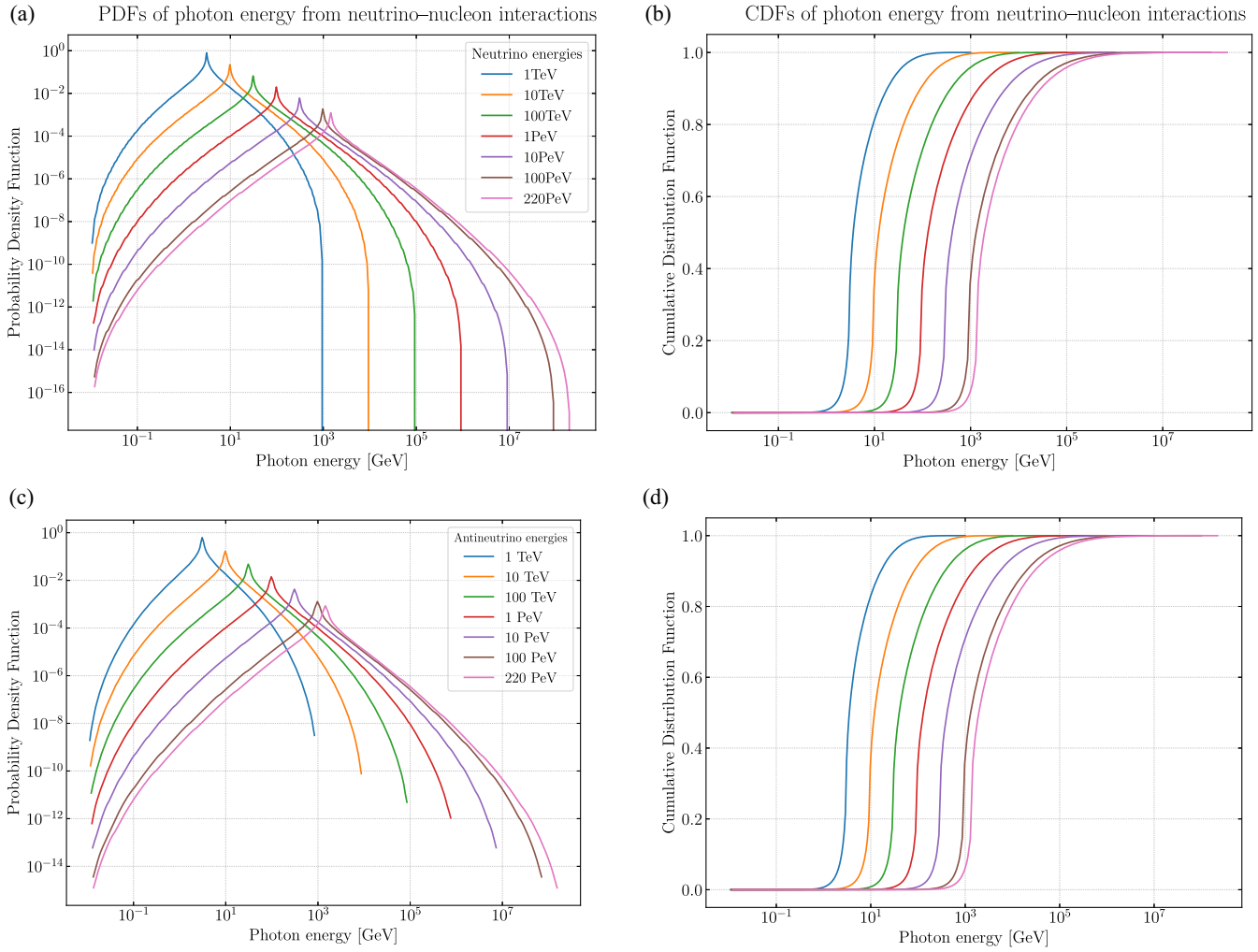

FIG. 3. Photon energy distributions generated by neutrino–nucleon and antineutrino–nucleon scattering. The upper panels show the probability density (left) and cumulative distribution (right) for neutrinos, while the lower panels present the corresponding distributions for antineutrinos. The results demonstrate that TeV–PeV photons are produced with significant probability in both cases. (a) PDFs of photon energy from neutrino–nucleon interactions. (b) CDFs of photon energy from neutrino–nucleon interactions. (c) PDFs of photon energy from antineutrino–nucleon interactions. (d) CDFs of photon energy from antineutrino–nucleon interactions.

$$E_{\rm sym}^{\rm lab}=\sqrt{\frac{1+v}{1-v}}\frac{m_\pi}{2}=\sqrt{\frac{2E_\nu^{\rm lab}+m_N}{m_N}}\frac{m_\pi}{2}\simeq\sqrt{\frac{E_\nu^{\rm lab}}{2m_N}}m_\pi, \quad (38)$$

which increases with $E_\nu^{\rm lab}$, as seen in Fig. 3.

Next, we analyze the upper and lower bounds of $E_\gamma^{\rm lab}$ in the photon probability density function $f(E_\gamma^{\rm lab}|E_\nu^{\rm lab})$. From Eqs. (30) to (33), we observe that, in addition to the lower bound $p_{\rm low}^{\nu N}$, the integral in Eq. (30) also has an upper bound, $p_{\rm up}^{\nu N}$, given by,

$$p_{\rm up}^{\nu N}=E_\nu^{\nu N}. \quad (39)$$

Thus, if $p_{\rm low}^{\nu N}>p_{\rm up}^{\nu N}$, the integral in Eq. (30) vanishes and then $f=0$. The condition $p_{\rm low}^{\nu N}<p_{\rm up}^{\nu N}$ yields the allowed photon-energy window

$$\frac{\sqrt{(E_\nu^{\nu N})^2+m_\pi^2}-E_\nu^{\nu N}}{2}<E_\gamma^{\nu N}<\frac{\sqrt{(E_\nu^{\nu N})^2+m_\pi^2}+E_\nu^{\nu N}}{2}. \quad (40)$$

In the limit $E_\nu^{\nu N}\gg m_\pi$, this reduces to

$$\frac{m_\pi^2}{4E_\nu^{\nu N}}<E_\gamma^{\nu N}<E_\nu^{\nu N}. \quad (41)$$

Boosting to the laboratory frame, Eqs. (34) and (35) give the upper bound

$$E_{\rm up}^{\rm lab}=E_\nu^{\rm lab}, \quad (42)$$

i.e., the photon energy cannot exceed the incident (anti) neutrino energy. The lower bound becomes

$$E_{\rm low}^{\rm lab} = \frac{m_\pi^2}{4E_\nu^{\rm lab}}\left(\frac{1+v}{1-v}\right) = \frac{m_\pi^2}{4E_\nu^{\rm lab}}\frac{2E_\nu^{\rm lab}+m_N}{m_N} \simeq \frac{m_\pi^2}{2m_N}, \quad (43)$$

which is independent of $E_\nu^{\rm lab}$ and numerically equals 9.7×10^{-3} GeV, as clearly depicted in the left panels of Fig. 3.

Based on the energies of (anti)neutrinos recorded by IceCube and KM3NeT, which may originate from dense astrophysical environments, we investigate whether UHE incident (anti)neutrinos can produce UHE photons through scattering with nucleons. Our calculations show that, for an incident (anti)neutrino with energy $E_\nu^{\rm lab}$, the highest probability corresponds to producing photons with energies of approximately $0.10\times\sqrt{E_\nu^{\rm lab}/\text{GeV}}$ GeV. Meanwhile, for incident (anti)neutrinos with energies above 1 TeV, the probability of producing photons with energies exceeding 1 GeV is greater than 99%. For incident (anti)neutrinos with energies above 1 PeV, the probability of producing photons with energies exceeding 1 TeV is greater than 13%. For incident 220 PeV (anti)neutrinos, the probability of producing photons with energies exceeding 1 TeV is greater than 94%.

In dense astrophysical environments such as the interior of Wolf–Rayet stars that serve as GRB progenitors, the secondary photons produced by this reaction are essentially unobservable if the interaction occurs in an optically thick region. However, if it takes place in an optically thin region, the resulting UHE photons may escape and become detectable. This motivates a concrete application to the preburst of GRB, which we quantify in the next section.

IV. APPLICATION TO THE PREBURST PHOTONS OF GRB 221009A

In this section, we apply this mechanism to a concrete astrophysical phenomenon that remains to be understood. A natural case study is the preburst emission of GRB 221009A. As shown in Fig. 6, the KM2A detector of LHAASO observed four photons at TeV band prior to the main prompt emission, and even before the Fermi-GBM trigger time t_0, with their arrival times distributed between $t_0-69.1$ s and $t_0-19.8$ s [33–35]. These events have not yet received a widely accepted explanation within conventional prompt or afterglow frameworks [36].

For the scenario considered here, neutrinos are produced while the jet is still propagating inside the progenitor. Photons generated in the same inner region are trapped due to the large optical depth, whereas neutrinos can escape efficiently. Such a precursor neutrino component is also supported by studies of GRB-associated neutrinos observed by IceCube [37,38]. These escaping neutrinos subsequently interact with protons and neutrons in the optically thin outer region of the hydrogen (H) envelope, producing π^0 and, through their decay, UHE photons via the mechanism described in Secs. II and III. As a consequence, these (anti)neutrino-produced photons can manifest as a separated precursor signal.

To quantify this picture, we adopt the jet-head propagation framework of Refs. [39,40]. In the H envelope, the Lorentz factor of the jet head is given by

$$\Gamma_h = 3\frac{L_{52}^{1/4}}{r_{12}^{1/2}\rho_{-7}^{1/4}}, \quad (44)$$

where the dimensionless quantities are defined as

$$r_{12} \equiv \frac{r}{10^{12}\ \text{cm}}, \quad (45)$$

$$\rho_{-7} \equiv \frac{\rho}{10^{-7}\ \text{g}\cdot\text{cm}^{-3}}, \quad (46)$$

$$L_{52} \equiv \frac{L_{\rm iso}}{10^{52}\ \text{erg/s}}. \quad (47)$$

Here r is the shock radius, $L_{\rm iso}$ is the isotropic jet luminosity, and ρ denotes the density of the H envelope at radius r.

For the jet propagation, we assume a constant isotropic luminosity $L_{\rm iso}=10^{52}L_0\,\text{erg}\,\text{s}^{-1}$ and a power-law density profile,

$$\rho(r) = 10^{-7}\rho_0\left(\frac{r}{10^{12}\ \text{cm}}\right)^{-k}\ \text{g}\,\text{cm}^{-3}, \quad (48)$$

where the index k is typically in the range 2.0–2.5 [41].

Under these assumptions, the jet-head Lorentz factor and velocity become

$$\Gamma_h = 3\left(\frac{L_0}{\rho_0}\right)^{1/4} r_{12}^{(k-2)/4}, \quad (49)$$

$$v_h = c\sqrt{1-\Gamma_h^{-2}} = c\sqrt{1-\frac{1}{A_0 r_{12}^{(k-2)/2}}}, \quad (50)$$

where $A_0 \equiv 9(L_0/\rho_0)^{1/2}$.

If a (anti)neutrino is produced when the jet head is at radius $r_{\rm gen}$, the corresponding lead time relative to photons emitted only after jet breakout is

$$T = \int_{r_{\rm gen}}^{R}\frac{dr'}{v_h} - \int_{r_{\rm gen}}^{R}\frac{dr'}{c} = 33\ \text{s}\int_{r_{\rm gen,12}}^{R_{12}}\left[\frac{1}{\sqrt{1-A_0^{-1}(r'_{12})^{-(k-2)/2}}}-1\right]dr'_{12}, \quad (51)$$

where we have defined

$$R_{12} \equiv \frac{R}{10^{12}\ \mathrm{cm}}, \qquad r_{\mathrm{gen},12} \equiv \frac{r_{\mathrm{gen}}}{10^{12}\ \mathrm{cm}}. \tag{52}$$

Here R is the outer radius of the H envelope.

Following Ref. [39], the (anti)neutrino energy in the laboratory frame is

$$\begin{aligned} E_\nu^{\mathrm{lab}} &\simeq 2\left(\frac{1+z}{2}\right)^{-1}\Gamma_h^{3/2} r_{\mathrm{gen},12}^{1/2} L_0^{-1/4}\ \mathrm{TeV} \\ &= 18 B_0 r_{\mathrm{gen},12}^{(3k-2)/8}\ \mathrm{TeV}, \end{aligned} \tag{53}$$

where $B_0 \equiv L_0^{1/8}\rho_0^{-3/8}$, and in the second line we have used the redshift $z = 0.151$ for GRB 221009A [42].

The generation probability of precursor (anti)neutrinos is derived to follow the standard E_ν^{-2} spectrum [39],

$$P_{\mathrm{gen}}(T) \propto [E_\nu^{\mathrm{lab}}(T)]^{-2}. \tag{54}$$

The probability that such a (anti)neutrino propagates to the optically thin region without further absorption is given by

$$\begin{aligned} P_{\mathrm{pro}}^{(a)}(T) &\propto \frac{\exp\left[-\int_{r_{\mathrm{gen}}(T)}^{R} n(r')\sigma_a(E_\nu^{\mathrm{lab}}(r'))\mathrm{d}r'\right]}{[R - r_{\mathrm{gen}}(T)]^2}, \\ &\propto \frac{e^{-6\rho_0\int_{r_{\mathrm{gen},12}(T)}^{R_{12}}(r'_{12})^{-k}\sigma_{-28}(r'_{12})\mathrm{d}r'_{12}}}{[R_{12} - r_{\mathrm{gen},12}(T)]^2} \end{aligned} \tag{55}$$

where $a = \nu, \bar{\nu}$ labels neutrinos and antineutrinos, $n(r)$ is the nucleon number density,

$$n(r) = 6\times 10^{16}\ \mathrm{cm}^{-3}\rho_0\left(\frac{r}{10^{12}\ \mathrm{cm}}\right)^{-k}, \tag{56}$$

and σ_a denotes the total νN (or $\bar{\nu}N$) cross section obtained in this work (see Fig. 4). The exponential factor in Eq. (55) accounts for attenuation due to (anti)neutrino–nucleon interactions along the propagation path, while the denominator reflects the geometric dilution of the (anti)neutrino flux, which follows an inverse-square law with distance.

Finally, the observable joint distribution of precursor photons can be written as

$$\mathcal{P}(T, E_\gamma^{\mathrm{lab}}) \propto \sum_{a=\nu,\bar{\nu}} P_{\mathrm{gen}}(T) P_{\mathrm{pro}}^{(a)}(T) f_a(E_\gamma^{\mathrm{lab}}|E_\nu^{\mathrm{lab}}(T)), \tag{57}$$

where $f_a(E_\gamma^{\mathrm{lab}}|E_\nu^{\mathrm{lab}})$ is the photon energy distribution analyzed in Secs. II and III. This expression provides a factorized description of the full process, combining the neutrino production, propagation, and conversion into observable photons. In the numerical application below, Eq. (53) implies that $E_\nu^{\mathrm{lab}} \sim \mathcal{O}(10)$ TeV throughout the relevant region of the envelope, consistent with the preburst observations of GRB 221009A.

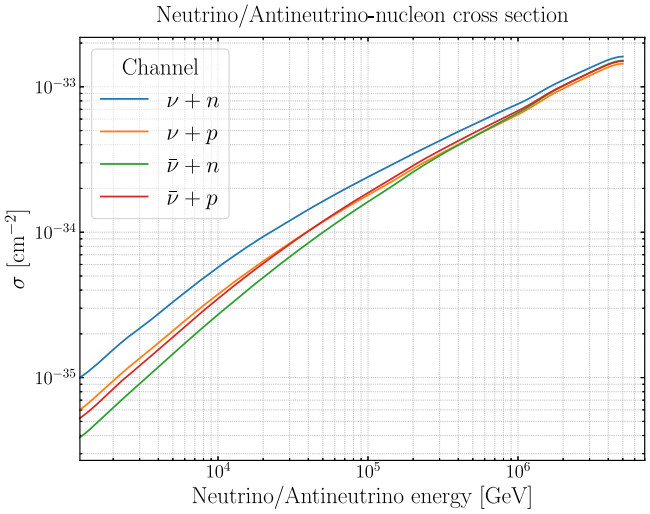

FIG. 4. Total (anti)neutrino-nucleon cross sections as functions of the (anti)neutrino energy, including the channels $\nu + n$ (blue), $\nu + p$ (orange), $\bar{\nu} + n$ (green), and $\bar{\nu} + p$ (red). Here all final states are included, rather than only those leading to pion production.

In the numerical calculation, we adopt the benchmark parameters $L_0 = 1$, $\rho_0 = 10$, and $R_{12} = 20$, and assume that the inner radius of the H envelope is $\sim 10^{11}$ cm. In this parameter regime, the total νN and $\bar{\nu}N$ cross sections increase from $\sim 10^{-35}$ cm^2 to $\sim 10^{-34}$ cm^2, as shown in Fig. 4.

The left and right panels of Fig. 5 show the resulting lead-time distributions for different values of k for PDF and CDF, respectively, where we define $T_{\mathrm{obs}} \equiv -T$ so that preburst photons correspond to negative observed times relative to the trigger time at $T_{\mathrm{obs}} = t_0 = 0$ s. The maximum lead time is $T_{\mathrm{max}} \simeq 180$ s. The distribution is strongly weighted toward short lead times. This behavior arises

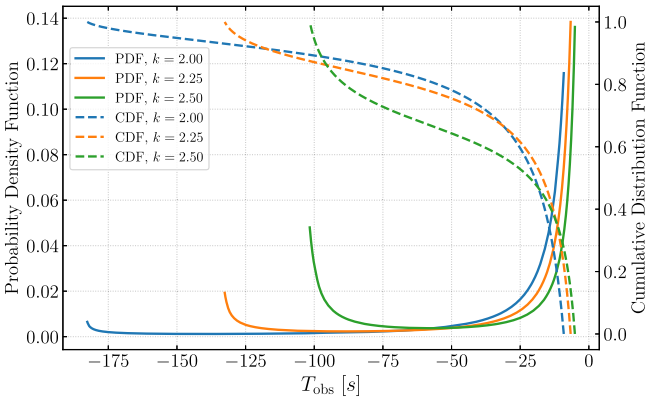

FIG. 5. Lead-time distribution for GRB 221009A. Solid curves: normalized probability density of the lead time $T_{\mathrm{obs}} \equiv -T$ for $k = 2.00$ (blue), $k = 2.25$ (orange), and $k = 2.50$ (green). Dashed curves: corresponding cumulative distribution functions. The benchmark parameters are $L_0 = 1$, $\rho_0 = 10$, and $R_{12} = 20$.

because a smaller T corresponds to a larger production radius $r_{\rm gen}$ [see Eq. (51)], which in turn leads to a larger propagation probability $P^{(a)}_{\rm pro}(T)$ [see Eq. (55)].

At the same time, the distribution exhibits a mild enhancement at large T. This can be understood as follows: a larger T corresponds to a smaller neutrino energy $E^{\rm lab}_\nu$ [see Eqs. (51) and (53)], and hence to a larger generation probability $P_{\rm gen}(T)$ [see Eq. (54)].

As a result of these competing effects, the distribution develops a long tail extending to $\mathcal{O}(10^2)$ s. This naturally allows for precursor signals appearing tens of seconds prior to the prompt emission in this scenario.

To facilitate a direct comparison with observational data, we define $E_{\rm obs} \equiv E^{\rm lab}_\gamma$ and focus on the LHAASO-relevant energy window $E_{\rm obs} = 4$–10 TeV. The resulting relative probability density, normalized to its maximum within the displayed window, is shown in Fig. 6. The distribution exhibits a pronounced high-probability ridge extending across photon energies of a few TeV and lead times of several tens of seconds.

As shown in Fig. 6, all four LHAASO preburst events fall within the predicted support of the distribution and overlap with the main high-probability region. This indicates that the (anti)neutrino-induced photon production mechanism studied here can quantitatively account for the observed preburst window of GRB 221009A. We emphasize that this mechanism is not necessarily unique. Rather, it provides a viable precursor channel in which (anti)neutrinos escape from the optically thick inner region and subsequently convert into photons in the outer optically thin envelope, leading to a precursor signal.

V. DISCUSSION AND SUMMARY

In this work, we investigated the production of high-energy photons via the neutrino–nucleon scattering process followed by π^0 decay. By calculating the neutrino–parton cross sections, incorporating nucleon PDFs and pion fragmentation functions, and evaluating the decay rates of π^0 into photons, we obtained the photon energy distributions for incident (anti)neutrinos with energies ranging from 1 TeV to 220 PeV. The results indicate that this process can efficiently produce UHE photons, with nearly identical outcomes for neutrinos and antineutrinos. We further analyzed the resulting photon energy spectra and found that for (anti)neutrinos with energies above 1 PeV, the probability of producing photons exceeding 1 TeV is greater than 13%—a non-negligible fraction that supports potential observational relevance.

In dense astrophysical environments such as the jets of active galactic nuclei [10], the internal shocks of GRBs [9],

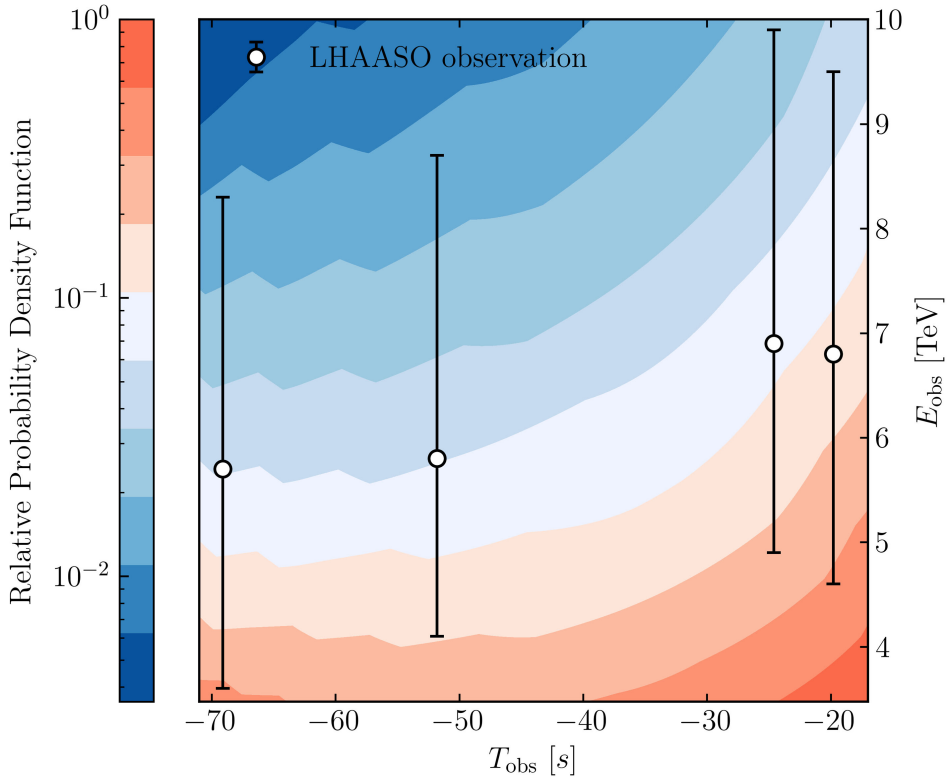

FIG. 6. Relative two-dimensional probability density in the observed $(T_{\rm obs}, E_{\rm obs})$ plane, normalized to its maximum within the displayed region. The benchmark parameters are $k = 2.5$, $L_0 = 1$, $\rho_0 = 10$, and $R_{12} = 20$. The data points with error bars indicate the reported LHAASO preburst photons of GRB 221009A. All points lie within the main high-probability region of the predicted distribution.

and the outer layers of core-collapse supernovae [11–13], UHE neutrinos can be copiously produced through hadronic interactions of accelerated protons with ambient matter or radiation fields. If a fraction of these neutrinos traverse regions of moderate density, where the optical depth is low enough for photons to escape, the mechanism investigated in this work can operate efficiently. Under such conditions, UHE neutrinos may generate secondary photons via neutral pion decay following νN scattering, adding a subdominant but potentially observable component to the overall gamma-ray flux.

Our results quantitatively demonstrate that this process, while contributing only a small fraction of the total emission, could nonetheless produce detectable high-energy photons under favorable conditions. As a concrete example, the observed preburst of GRB 221009A, characterized by photon energies of a few TeV and lead times of several tens of seconds [35,43–46], can be naturally accommodated within our framework. By combining the neutrino production, propagation, and conversion processes, our model provides a self-consistent quantitative description of both the energy scale and the temporal structure of the preburst signal. In this sense, the mechanism developed in this work is not merely a theoretical possibility, but can be applied to a concrete astrophysical scenario.

We have also estimated the luminosity of neutrinos L_ν, and that of the parent protons L_p, required to reproduce the LHAASO preburst events. For the benchmark neutrino-nucleon cross section and envelope parameters considered in this work, the required precursor-neutrino luminosity lies within a reasonable range for an exceptionally energetic burst such as GRB 221009A. The corresponding parent-proton luminosity depends mainly on the neutrino-production efficiency, defined by $E^{\rm req}_{\nu,{\rm iso}} = \xi_\nu E^{\rm req}_{p,{\rm iso}}$. For typical values of ξ_ν adopted in GRB-neutrino estimates, the required isotropic-equivalent parent-proton energy remains comparable to or below the available isotropic-equivalent energy budget of GRB 221009A. This normalization check therefore supports the energetic consistency of the proposed preburst neutrino-induced photon scenario within the benchmark parameter region considered here.

The associated multiwavelength electromagnetic emission is also expected to remain consistent with observations. The photons produced together with the precursor neutrinos are generated before jet breakout, inside the dense stellar envelope, where both the primary TeV photons and the lower-energy cascade photons are efficiently trapped. The absorbed electromagnetic energy is therefore released only on a much longer diffusion timescale and is softened by repeated scattering and partial thermalization, rather than escaping promptly as an x-ray or GeV counterpart to the LHAASO preburst photons. In addition, Swift/XRT did not observe the GRB field during the preburst time window of GRB 221009A [47]. Although Fermi-GBM and Fermi-LAT observed GRB 221009A after the trigger during the prompt phase, the expected escaping cascade flux associated with the preburst phase is far below the relevant triggering or detection thresholds of these instruments [48,49]. Thus, while a full cascade and radiation-transfer calculation is beyond the scope of this work, our order-of-magnitude estimates indicate that the benchmark scenario is compatible with the available multiwavelength observations.

This work establishes a new quantitative pathway linking high-energy neutrino interactions to gamma-ray emission, expanding our understanding of multimessenger astrophysics in extreme environments. The consistency between neutrino and antineutrino photon production further simplifies observational predictions, highlighting the potential of this process to constrain neutrino origins and astrophysical environment properties through future multiwavelength and multimessenger surveys.

ACKNOWLEDGMENTS

We thank the anonymous referee for valuable comments and suggestions. This work is supported by the National Natural Science Foundation of China under Grant No. 12335006 and No. 12675108. This work is also supported by the High-performance Computing Platform of Peking University.

DATA AVAILABILITY

There are no publicly available research data or software supporting this manuscript. Requests for further information or data should be sent to the authors.

APPENDIX: AMPLITUDE SQUARE OF THE NEUTRINO-PARTON SCATTERING

In this appendix we collect the squared amplitudes for all neutrino–parton and antineutrino-parton scattering processes. Owing to the generation structure of the electroweak interaction, it is sufficient to present the results for the first generation. The corresponding expressions for second- and third-generation leptons and quarks are obtained by replacing the masses and the relevant CKM matrix elements in the formulas below.

The tree-level Feynman diagrams for all processes are shown in Fig. 7, where the left column corresponds to neutrino-induced channels and the right column to antineutrino-induced channels.

The squared amplitudes for the processes with an initial neutrino are

$$|\mathcal{M}_{d,u}|^2 = |V_{ud}|^2 \frac{e^4}{\sin^4\theta_w} \times \frac{P_\nu \cdot P_i (m_d^2 - m_e^2 - m_u^2 + 2P_\nu \cdot P_i)}{(m_W^2 - m_e^2 + 2P_\nu \cdot P_l)^2}, \quad \text{(A1)}$$

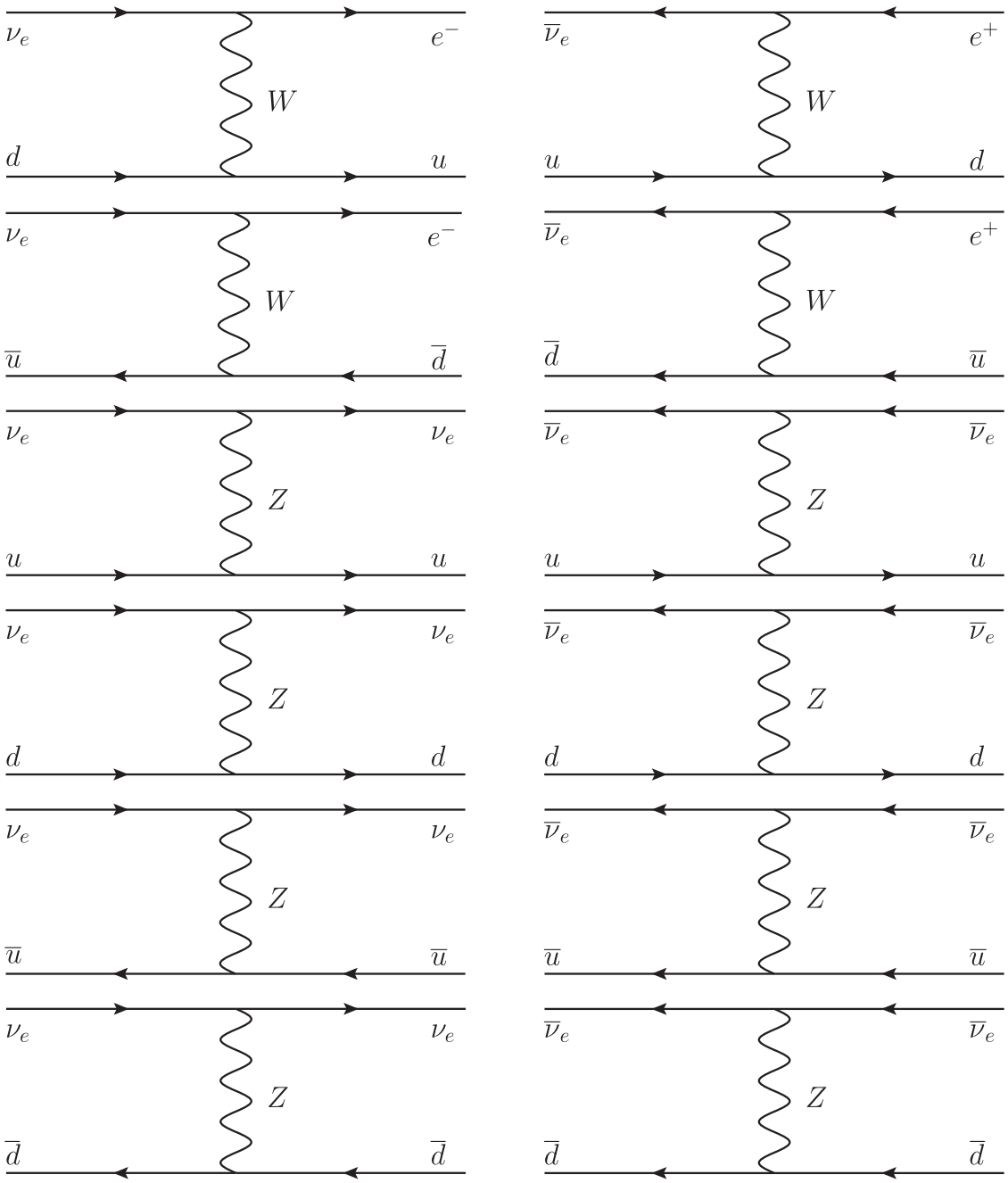

FIG. 7. Feynman diagrams for neutrino–parton and antineutrino–parton scattering. Diagrams in the left column correspond to neutrino-induced processes, while those in the right column correspond to antineutrino-induced processes.

$$|\mathcal{M}_{\bar{u},\bar{d}}|^2 = |V_{ud}|^2 \frac{e^4}{\sin^4\theta_w}(P_\nu \cdot P_i - P_\nu \cdot P_l) \times \frac{(m_e^2 + m_u^2 - m_d^2 + 2P_\nu \cdot P_i - 2P_\nu \cdot P_l)}{(m_W^2 - m_e^2 + 2P_\nu \cdot P_l)^2}, \tag{A2}$$

$$|\mathcal{M}_{u,u}|^2 = \frac{e^4}{\cos^4\theta_w}\frac{1}{18(m_Z^2 + 2P_\nu \cdot P_l)^2} \times [4P_\nu \cdot P_l(m_u^2(3\csc^2\theta_w - 4) - 8P_\nu \cdot P_i) + (9\csc^4\theta_w - 24\csc^2\theta_w + 32)(P_\nu \cdot P_i)^2 + 16(P_\nu \cdot P_l)^2], \tag{A3}$$

$$|\mathcal{M}_{d,d}|^2 = \frac{e^4}{\cos^4\theta_w}\frac{1}{18(m_Z^2+2P_\nu\cdot P_l)^2} \times [2P_\nu\cdot P_l(m_d^2(3\csc^2\theta_w-2)-4P_\nu\cdot P_i) + (P_\nu\cdot P_i)^2\csc^4\theta_w(2\cos(2\theta_w)+\cos(4\theta_w)+6) + 4(P_\nu\cdot P_l)^2], \tag{A4}$$

$$|\mathcal{M}_{\bar{u},\bar{u}}|^2 = \frac{e^4}{\cos^4\theta_w\sin^4\theta_w}\frac{1}{18(m_Z^2+2P_\nu\cdot P_l)^2} \times [P_\nu\cdot P_l(4\cos^2\theta_w-1)(4m_u^2\sin^2\theta_w + (4\cos^2\theta_w-1)P_\nu\cdot P_l) + (P_\nu\cdot P_i)^2(4\cos(4\theta_w)-4\cos(2\theta_w)+9) - 2(P_\nu\cdot P_i)(P_\nu\cdot P_l)(4\cos^2\theta_w-1)^2], \tag{A5}$$

$$|\mathcal{M}_{\bar{d},\bar{d}}|^2 = \frac{e^4}{\cos^4\theta_w\sin^4\theta_w}\frac{1}{18(m_Z^2+2P_\nu\cdot P_l)^2} \times [P_\nu\cdot P_l(2\cos^2\theta_w+1)(2m_d^2\sin^2\theta_w + P_\nu\cdot P_l(2\cos^2\theta_w+1)) + (P_\nu\cdot P_i)^2(\cos(4\theta_w)+2\cos(2\theta_w)+6) - 2(P_\nu\cdot P_i)(P_\nu\cdot P_l)(2\cos^2\theta_w+1)^2]. \tag{A6}$$

The squared amplitudes for the processes with an initial antineutrino are

$$|\mathcal{M}_{u,d}|^2 = |V_{ud}|^2\frac{e^4}{\sin^4\theta_w}(P_\nu\cdot P_i - P_\nu\cdot P_l) \times\frac{(m_e^2+m_u^2-m_d^2+2P_\nu\cdot P_i-2P_\nu\cdot P_l)}{(m_W^2-m_e^2+2P_\nu\cdot P_l)^2}, \tag{A7}$$

$$|\mathcal{M}_{\bar{d},\bar{u}}|^2 = |V_{ud}|^2\frac{e^4}{\sin^4\theta_w} \times\frac{P_\nu\cdot P_i(m_d^2-m_e^2-m_u^2+2P_\nu\cdot P_i)}{(m_W^2-m_e^2+2P_\nu\cdot P_l)^2}, \tag{A8}$$

$$|\mathcal{M}_{u,u}|^2 = \frac{e^4}{\cos^4\theta_w\sin^4\theta_w}\frac{1}{18(m_Z^2+2P_\nu\cdot P_l)^2} \times [P_\nu\cdot P_l(4\cos^2\theta_w-1)(4m_u^2\sin^2\theta_w + (4\cos^2\theta_w-1)P_\nu\cdot P_l) + (P_\nu\cdot P_i)^2(4\cos(4\theta_w)-4\cos(2\theta_w)+9) - 2(P_\nu\cdot P_i)(P_\nu\cdot P_l)(4\cos^2\theta_w-1)^2], \tag{A9}$$

$$|\mathcal{M}_{d,d}|^2 = \frac{e^4}{\cos^4\theta_w\sin^4\theta_w}\frac{1}{18(m_Z^2+2P_\nu\cdot P_l)^2} \times [P_\nu\cdot P_l(2\cos^2\theta_w+1)(2m_d^2\sin^2\theta_w + P_\nu\cdot P_l(2\cos^2\theta_w+1)) + (P_\nu\cdot P_i)^2(\cos(4\theta_w)+2\cos(2\theta_w)+6) - 2(P_\nu\cdot P_i)(P_\nu\cdot P_l)(2\cos^2\theta_w+1)^2], \tag{A10}$$

$$|\mathcal{M}_{\bar{u},\bar{u}}|^2 = \frac{e^4}{\cos^4\theta_w}\frac{1}{18(m_Z^2+2P_\nu\cdot P_l)^2} \times [4P_\nu\cdot P_l(m_u^2(3\csc^2\theta_w-4)-8P_\nu\cdot P_i) + (9\csc^4\theta_w-24\csc^2\theta_w+32)(P_\nu\cdot P_i)^2 + 16(P_\nu\cdot P_l)^2], \tag{A11}$$

$$|\mathcal{M}_{\bar{d},\bar{d}}|^2 = \frac{e^4}{\cos^4\theta_w}\frac{1}{18(m_Z^2+2P_\nu\cdot P_l)^2} \times [2P_\nu\cdot P_l(m_d^2(3\csc^2\theta_w-2)-4P_\nu\cdot P_i) + (P_\nu\cdot P_i)^2\csc^4\theta_w(2\cos(2\theta_w)+\cos(4\theta_w)+6) + 4(P_\nu\cdot P_l)^2]. \tag{A12}$$

Finally, substituting Eqs. (17), (18), and (22) into the expressions above, and neglecting lepton and parton masses, we are able to obtain the final forms of $|\mathcal{M}_{i,i'}|^2$ in the νN frame.

[1] S. Aiello *et al.*, Observation of an ultra-high-energy cosmic neutrino with KM3NeT, Nature (London) **638**, 376 (2025); **640**, E3(E) (2025).

[2] IceCube Collaboration, Evidence for high-energy extraterrestrial neutrinos at the IceCube detector, Science **342**, 1242856 (2013).

[3] M. G. Aartsen *et al.*, Observation of high-energy astrophysical neutrinos in three years of IceCube data, Phys. Rev. Lett. **113**, 101101 (2014).

[4] D. D. Dzhappuev *et al.*, Carpet-3 detection of a photonlike air shower with estimated primary energy above 100 TeV in a spatial and temporal coincidence with GRB 221009A, Phys. Rev. D **111**, 102005 (2025).

[5] Z. Cao *et al.*, Ultrahigh-energy photons up to 1.4 petaelectronvolts from 12 γ-ray Galactic sources, Nature (London) **594**, 33 (2021).

[6] M. Amenomori *et al.*, First detection of photons with energy beyond 100 TeV from an astrophysical source, Phys. Rev. Lett. **123**, 051101 (2019).

[7] H. Abe *et al.*, MAGIC observations provide compelling evidence of hadronic multi-TeV emission from the putative PeVatron SNR G106.3 + 2.7, Astron. Astrophys. **671**, A12 (2023).

[8] C. A. Argüelles, F. Halzen, and N. Kurahashi, From the dawn of neutrino astronomy to a new view of the extreme universe, Phys. Rev. X **15**, 030501 (2025).
[9] K. Murase and K. Ioka, TeV–PeV neutrinos from low-power gamma-ray burst jets inside stars, Phys. Rev. Lett. **111**, 121102 (2013).
[10] C. D. Dermer, K. Murase, and Y. Inoue, Photopion production in black-hole jets and flat-spectrum radio quasars as PeV neutrino sources, J. High Energy Astrophys. **3–4**, 29 (2014).
[11] A. M. Bykov, D. C. Ellison, P. E. Gladilin, and S. M. Osipov, Ultrahard spectra of PeV neutrinos from supernovae in compact star clusters, Mon. Not. R. Astron. Soc. **453**, 113 (2015).
[12] S. Chakraborty and I. Izaguirre, Diffuse neutrinos from extragalactic supernova remnants: Dominating the 100 TeV IceCube flux, Phys. Lett. B **745**, 35 (2015).
[13] M. Petropoulou, S. Coenders, G. Vasilopoulos, A. Kamble, and L. Sironi, Point-source and diffuse high-energy neutrino emission from type IIn supernovae, Mon. Not. R. Astron. Soc. **470**, 1881 (2017).
[14] J. G. Learned and K. Mannheim, High-energy neutrino astrophysics, Annu. Rev. Nucl. Part. Sci. **50**, 679 (2000).
[15] Z. Cao, S. Chen, R. Liu, and R. Yang, Ultra-high-energy gamma-ray astronomy, Annu. Rev. Nucl. Part. Sci. **73**, 341 (2023).
[16] R. Gill and J. Granot, Gamma-ray bursts at TeV energies: Theoretical considerations, Galaxies **10**, 74 (2022).
[17] K. Hirata *et al.*, Observation of a neutrino burst from the supernova SN 1987A, Phys. Rev. Lett. **58**, 1490 (1987).
[18] J. N. Bahcall and R. K. Ulrich, Solar models, neutrino experiments and helioseismology, Rev. Mod. Phys. **60**, 297 (1988).
[19] M. G. Aartsen *et al.*, Multimessenger observations of a flaring blazar coincident with high-energy neutrino IceCube-170922A, Science **361**, eaat1378 (2018).
[20] S. Ansoldi *et al.*, The blazar TXS 0506 + 056 associated with a high-energy neutrino: Insights into extragalactic jets and cosmic ray acceleration, Astrophys. J. Lett. **863**, L10 (2018).
[21] S. Navas *et al.*, Review of particle physics, Phys. Rev. D **110**, 030001 (2024).
[22] C. Schmidt, J. Pumplin, D. Stump, and C. P. Yuan, CT14QED parton distribution functions from isolated photon production in deep inelastic scattering, Phys. Rev. D **93**, 114015 (2016).
[23] K. Xie, B. Zhou, and T. J. Hobbs, The photon content of the neutron, J. High Energy Phys. 04 (2024) 022.
[24] C. Lorcé, A. Metz, B. Pasquini, and P. Schweitzer, Parton distribution functions and their generalizations, Encycl. Part Phys. **2**, 167 (2026).
[25] D. de Florian, R. Sassot, and M. Stratmann, Global analysis of fragmentation functions for pions and kaons and their uncertainties, Phys. Rev. D **75**, 114010 (2007).
[26] D. de Florian, R. Sassot, and M. Stratmann, Global analysis of fragmentation functions for protons and charged hadrons, Phys. Rev. D **76**, 074033 (2007).
[27] D. de Florian, R. Sassot, M. Epele, R. J. Hernández-Pinto, and M. Stratmann, Parton-to-pion fragmentation reloaded, Phys. Rev. D **91**, 014035 (2015).
[28] Q. Peng and B.-Q. Ma, Determination of meson fragmentation functions in the field-Feynman model, Phys. Rev. C **107**, 055202 (2023).
[29] J. Gao, X. Shen, H. Xing, Y. Zhao, and B. Zhou, Fragmentation functions of charged hadrons at next-to-next-to-leading order and constraints on the proton parton distribution functions, Phys. Rev. Lett. **135**, 041902 (2025).
[30] H. Suzuki, Neutrinos from core-collapse supernova explosions, Prog. Theor. Exp. Phys. **2024**, 05B101 (2024).
[31] A. Dar, High-energy cosmic rays, gamma-rays and neutrinos from jetted GRBs, in: *8th International Workshop on Neutrino Telescopes* (Papergraf, Padova, 1999).
[32] E. Nakar, A unified picture for low-luminosity and long gamma-ray bursts based on the extended progenitor of *ll*GRB 060218/SN 2006AJ, Astrophys. J. **807**, 172 (2015).
[33] Z. Cao *et al.*, Very high-energy gamma-ray emission beyond 10 TeV from GRB 221009A, Sci. Adv. **9**, adj2778 (2023).
[34] Z. Cao *et al.*, A tera–electron volt afterglow from a narrow jet in an extremely bright gamma-ray burst, Science **380**, adg9328 (2023).
[35] Q. Liu, H. Song, and B.-Q. Ma, Direct evidence for preburst stage of gamma-ray burst from GRB 221009A data, Res. Notes Am. Astron. Soc. **8**, 263 (2024).
[36] B. Stern and I. Tkachev, GRB 221009A, its precursor, and two afterglows in the Fermi data, JETP Lett. **118**, 553 (2023).
[37] Y. Huang, H. Li, and B.-Q. Ma, Consistent Lorentz violation features from near-TeV IceCube neutrinos, Phys. Rev. D **99**, 123018 (2019).
[38] Y. Huang and B.-Q. Ma, Ultra-high energy cosmic neutrinos from gamma-ray bursts, Fundam. Res. **4**, 51 (2024).
[39] P. Meszaros and E. Waxman, TeV neutrinos from successful and choked gamma-ray bursts, Phys. Rev. Lett. **87**, 171102 (2001).
[40] S. Razzaque, P. Meszaros, and E. Waxman, Neutrino tomography of gamma ray bursts and massive stellar collapses, Phys. Rev. D **68**, 083001 (2003).
[41] M. Bhattacharya, J. A. Carpio, K. Murase, and S. Horiuchi, High-energy neutrino emission from magnetised jets of rapidly rotating protomagnetars, Mon. Not. R. Astron. Soc. **521**, 2391 (2023).
[42] S. Lesage *et al.*, Fermi-GBM discovery of GRB 221009A: An extraordinarily bright GRB from onset to afterglow, Astrophys. J. Lett. **952**, L42 (2023).
[43] H. Song and B.-Q. Ma, Energy-dependent intrinsic time delay of gamma-ray bursts on testing Lorentz invariance violation, Phys. Lett. B **856**, 138951 (2024).
[44] H. Song and B.-Q. Ma, Examining Lorentz invariance violation with three remarkable GRB photons, Phys. Dark Universe **47**, 101808 (2025).
[45] H. Song and B.-Q. Ma, Lorentz invariance violation from gamma-ray bursts, Astrophys. J. **983**, 9 (2025).
[46] H. Song and B.-Q. Ma, Carpet-3 300 TeV photon event as an evidence for Lorentz violation, Phys. Lett. B **870**, 139959 (2025).
[47] M. A. Williams *et al.*, GRB 221009A: Discovery of an exceptionally rare nearby and energetic gamma-ray burst, Astrophys. J. Lett. **946**, L24 (2023).
[48] C. Meegan *et al.*, The Fermi gamma-ray burst monitor, Astrophys. J. **702**, 791 (2009).
[49] L. Nava, R. Desiante, F. Longo, A. Celotti, N. Omodei, G. Vianello, E. Bissaldi, and T. Piran, Constraints on the bulk Lorentz factor of gamma-ray burst jets from Fermi/LAT upper limits, Mon. Not. R. Astron. Soc. **465**, 811 (2017).